Myelin development in visual scene-network tracts beyond late childhood: A multimodal neuroimaging study

Tobias W. Meissner[a,b], Erhan Genç[c], Burkhard Mädler[d], Sarah Weigelt[a]

[a] TU Dortmund University, Faculty of Rehabilitation Sciences, Department of Vision, Visual Impairments & Blindness, Emil-Figge-Str. 50, 44227 Dortmund, Germany

[b] Ruhr University Bochum, Faculty of Psychology, Universitätsstr. 150, 44801 Bochum, Germany

[c] Ruhr University Bochum, Faculty of Psychology, Institute for Cognitive Neuroscience, Department of Biopsychology, Universitätsstr. 150, 44801 Bochum, Germany

[d] Philips GmbH, Health Systems Department, Hamburg, Germany

Corresponding author: Tobias W. Meissner, tobias.meissner@rub.de

Email of co-authors: EG: erhan.genc@rub.de, BM: burkhard.maedler@philips.com, SW: sarah.weigelt@tu-dortmund.de

Highlights

- Myelin in intrahemispheric scene-network tracts increases beyond late childhood
- OPA-hippocampus tracts also show prolonged myelination
- Diffusion tensor imaging parameters do not mirror myelin water fraction results

Abstract

The visual scene-network—comprising the parahippocampal place area (PPA), retrosplenial cortex (RSC), and occipital place area (OPA)—shows a prolonged functional development. Structural development of white matter that underlies the scene-network has not been investigated despite its potential influence on scene-network function. The key factor for white matter maturation is myelination. However, research on myelination using the gold standard method of post-mortem histology is scarce. *In vivo* alternatives diffusion-weighed imaging (DWI) and myelin water imaging (MWI) so far report broad-scale findings that prohibit inferences concerning the scene-network. Here, we combine MWI, DWI tractography, and fMRI to investigate myelination in scene-network tracts in middle childhood, late childhood, and adulthood. We report increasing myelin from middle childhood to adulthood in left RSC-OPA, and trends towards increases in the right RSC-OPA, left PPA-RSC and right PPA-OPA tracts. Moreover, tracts connecting the OPA to the key input region hippocampus showed myelin increases beyond late childhood. Our findings indicate that structural development coincides with functional development in the scene network, possibly enabling structure-function interactions.

Keywords

white matter, maturation, connectivity, diffusion weighed imaging, scene recognition, high-level vision

1 Introduction

The human cortical visual system contains three high-level areas that preferentially respond to scenes compared to other stimuli, e.g. objects or faces: the parahippocampal place area (PPA, Epstein & Kanwisher, 1998), the retrosplenial cortex (RSC, O'Craven & Kanwisher, 2000), and the occipital place area (OPA, Grill-Spector, 2003; Hasson, Harel, Levy, & Malach, 2003). This functional network is strongly involved in scene processing (e.g. Bettencourt & Xu, 2013; Dilks, Julian, Kubilius, Spelke, & Kanwisher, 2011; Epstein, Higgins, Jablonski, & Feiler, 2007a), but also in orientation and navigation (e.g. Epstein, 2008; Julian, Ryan, Hamilton, & Epstein, 2016). The scene-network's components are already evident in middle childhood but at least for the PPA and the OPA there is evidence for a protracted development in terms of functional size and scene-selectivity beyond late childhood, possibly until adulthood (Chai, Ofen, Jacobs, & Gabrieli, 2010; Golarai et al., 2007; Meissner, Nordt, & Weigelt, 2019b).

Despite this commencing understanding of the developmental trajectory of scene-network function between middle childhood and adulthood, the development of the white matter structure underlying the scene-network has not received attention so far. However, white matter microstructure changes in corresponding brain areas were shown to be an underlying mechanism for specific cognitive development or differences, as has been evidenced for musical proficiency (Bengtsson et al., 2005), vocabulary development (Pujol et al., 2006), and many other cognitive abilities (for an overview see Fields, 2008). Thus, maturational status of scene-network white matter structure might influence scene-network gray matter functional development, or vice versa (Fields, 2015; Zatorre, Fields, & Johansen-Berg, 2012).

The PPA, RSC, and OPA contribute to the complex tasks of scene processing and navigation through (at least partially) distinct functional response properties (Baldassano, Esteva, Fei-Fei, & Beck, 2016a; Epstein & Higgins, 2007; Epstein, Parker, & Feiler, 2007b; Hutchison, Culham, Everling, Flanagan, & Gallivan, 2014; Vass & Epstein, 2013). Due to these distinct contributions, an efficient and mature transmission of signals between these areas is considered crucial for building an integrated perception of scenes. Further, the scene network does not work in an isolated fashion. On

the one hand, following the hierarchical organizational principle of the visual cortex, the early visual cortex (EVC) is a major input area to the PPA, RSC, and OPA (Grill-Spector & Malach, 2004). Unsurprisingly, studies in the past decades show that scene-selective areas are retinotopically organized and show strong functional connectivity to the EVC (Baldassano et al., 2016a; Baldassano, Fei-Fei, & Beck, 2016b; Epstein & Baker, 2019). On the other hand, recent evidence suggests that the hippocampus (HC) might be part of the scene-network or at least a major input-output region (Baldassano et al., 2016a; Baldassano, Beck, & Fei-Fei, 2013; Dalton, Zeidman, McCormick, & Maguire, 2018; Graham, Barense, & Lee, 2010; Hodgetts et al., 2017; Hodgetts, Shine, Lawrence, Downing, & Graham, 2016; Zeidman, Mullally, & Maguire, 2015). Consequently, an efficient signal transmission between the scene network areas and key areas working in concert with them to achieve scene perception should be an important developmental step.

Signal transmission can be optimized through increasing speed, synchrony, or reliability—all of which are mediated by increases in axon myelination (Miller, 1994; Zatorre et al., 2012). Axon myelination has traditionally been measured in post-mortem histological studies. However, post mortem-studies are rare in general and most studies focus on newborns' and young infants' gray matter myelin content. In the only histological study investigating white matter myelin development beyond middle childhood, the authors report tract-specific maturation patterns featuring peak myelin growth rates within the first two years after birth as well as continued maturation up middle childhood (Yakovlev & Lecours, 1967). Evidence for development beyond childhood was limited to intracortical neuropil and association areas but should be regarded as rather anecdotal due to the low number of investigated tracts and specimens in that age group.

Due to the very limited availability of specimens for post-mortem histological myelin assessment, the advance of diffusion-weighed imaging (DWI), a non-invasive magnetic resonance imaging (MRI) method that has the potential to inform about myelin *in vivo*, represented a milestone. DWI has since been applied to probe developmental changes in white matter myelination extensively. However, most studies focused on major long fiber tracts, such as the internal capsule or the corticospinal tract, that can be readily identified (semi-) automatically using brain atlases (e.g. Lebel &

Beaulieu, 2011; Mukherjee et al., 2001). As most long tracts are not directly involved in the visual scene-processing system and effects of age on white matter maturation were shown to be tract-specific (e.g. Rollins et al., 2010), the current literature is not informative on scene-network white matter development. Short-range tracts, which are crucial for relaying information in specialized functional networks over short distances, such as the scene-network, are understudied. The only relevant findings suggest ongoing myelination in temporal and parietal lobe short-range tracts (Oyefiade et al., 2018) or in white matter adjacent to dorsal and ventral visual stream cortical areas (Barnea-Goraly et al., 2005; Loenneker et al., 2011) and thus remain too unspecific for any inference on scene-network developmental trajectories.

DWI's sensitivity to myelin stems from its sensitivity to the diffusion of water because myelin reduces the inter-axonal space, increasing the anisotropy of water diffusion as a consequence (Feldman, Yeatman, Lee, Barde, & Gaman-Bean, 2010). However, several microstructural properties, such as axon diameter, axon packing density (Takahashi et al., 2002), axon membrane permeability (Ford, Hackney, Lavi, Phillips, & Patel, 1998), and fiber geometry (van Wedeen, Hagmann, Tseng, Reese, & Weisskoff, 2005) affect diffusion tensor imaging (DTI) parameters, too. Therefore, deducing myelination or maturational status from DTI parameters alone is challenging in most and even, in some cases, speculative (Jones, Knösche, & Turner, 2013).

Myelin water imaging (MWI, MacKay et al., 1994), another MRI technique, is sensitive to myelin, highly reproducible (Meyers et al., 2009), and not affected by other microstructural changes, (Laule et al., 2006; Laule et al., 2008; Moore et al., 2000). Thus, it gives a more direct estimation of the status of myelination than interpretation of DTI parameters alone. Yet, MWI has only recently become available in pediatric research settings, thanks to the implementation of parallel imaging (SENSE, Pruessmann, Weiger, Scheidegger, & Boesiger, 1999) and advances in sequence design (Deoni, Rutt, Arun, Pierpaoli, & Jones, 2008; Prasloski et al., 2012) which both drastically sped up acquisition time.

A series of MWI studies investigated infants and young children and found steep increases of myelin from birth to age two and a moderate increase thereafter (e.g. Dean et al., 2014; Dean et al.,

2015; Deoni et al., 2011; Deoni, Dean, O'Muircheartaigh, Dirks, & Jerskey, 2012; Deoni, Dean, Remer, Dirks, & O'Muircheartaigh, 2015). Recent findings indicate that while myelin does not seem to increase between middle and late childhood, a pronounced increase of myelin occurs in adolescence in major white matter tracts (Geeraert et al., 2018; Meissner, Genç, Mädler, & Weigelt, 2019a). However, scene-network specific data has not been analyzed until now.

To complement recent findings regarding the functional development of scene-network regions PPA, RSC, and OPA (Meissner et al., 2019b), we combined MWI and DWI-based probabilistic tractography to probe the structural maturation, i.e. myelin water fraction (MWF), of white matter that underlies scene-network function in middle childhood (7-8 years), late childhood (11-12 years), and adulthood (19-24 years). As previous behavioral studies identified a marked improvement in the performance in scene processing around the age of 10 (Day, 1975; Mackworth & Bruner, 1970; Munsinger & Gummerman, 1967; Vurpillot, 1968), these age groups were specifically chosen to capture the neural status—possibly underlying the behavior—before and after the change, as well as in a mature reference group. Further, we tested whether tracts that connect the scene-network with their key input/output areas such as the EVC or the HC, show increased myelination over time. In an extended analysis, we tested whether DWI parameters mirror our MWI results.

2 Methods

2.1 Participants

We analyzed data of 18 children aged 7-8 (*Mean (M)* = 7.56, *standard deviation (SD)* = 0.51; 7 female; henceforth: 7-8yo), 13 children aged 11-12 (*M* = 11.23, *SD* = 0.44; 8 female; henceforth: 11-12yo) and 16 adults aged 19-24 (*M* = 20.69, *SD* = 1.14; 7 female) for this study. The original sample included one additional 7-8yo that was excluded due to severely impaired data quality in the DWI scan, one 7-8yo that did not complete the myelin water imaging scan, and one 11-12yo, in which our localizer failed to reveal any scene-selective ROIs. Our study worked towards answering several associated research questions and included multiple MRI sequences. Thus, most participants‘ localizer data (see 2.2.2, Region of interest definition) was analyzed in a previous publication, which also holds detailed information on recruitment and compensation (Meissner et al., 2019b). All participants were healthy, had normal or corrected-to-normal vision, and had been born at term. No participant had past or current neurological or psychiatric conditions, or structural brain abnormalities.

2.2 Neuroimaging

All magnetic resonance images were acquired at the Neuroimaging Centre of the Research Department of Neuroscience at Ruhr University Bochum’s teaching hospital Bergmannsheil on a 3.0T Achieva scanner (Philips, Amsterdam, The Netherlands) using a 32-channel head coil. Acquisition of data reported in this manuscript was part of a longer protocol that included further functional scans. To reassure children and parents as well as to provide the possibility for low-threshold contact, children were accompanied by one of the experimenters in the scanner room throughout the entire procedure. Children who had not participated in an MRI study before were accustomed to the scanning environment, experimental procedure, and localizer task in a custom-built mock scanner at least one day prior to scanning. Participants were presented with short movie clips of a children’s TV program during the acquisition of structural MRI.

2.2.1 High-resolution anatomical imaging and cortical parcellation

To co-register magnetic resonance images from different sequence types (EPI, DWI, GRASE) as well as for gray-white matter segmentation and cortical parcellation, we acquired a T1-weighted high-resolution anatomical scan of the whole head (MP-RAGE, TR = 8.10 ms, TE = 3.72 ms, flip angle = 8°, 220 slices, matrix size = 240 × 240, voxel size = 1 mm × 1 mm × 1 mm). We excluded non-brain parts of the head using FSL BET (Smith, 2002).

We used FreeSurfer (RRID: SCR_001847, version 6.0.0) for automated cortical parcellation and segmentation of the T1-weighted images. The details of the applied recon-all analysis pipeline have been described elsewhere (Dale, Fischl, & Sereno, 1999; Fischl et al., 2002; Fischl et al., 2004; Fischl, Sereno, & Dale, 1999; Ségonne et al., 2004) and the procedure has been shown to be valid for all age groups in our study to the same extent (Ghosh et al., 2010).

To localize the EVC and the HC, we used FreeSurfer's implemented probabilistic atlases (Fischl et al., 2008). For the EVC, atlases for the primary and secondary visual area (V1 and V2) were used. We converted V1, V2, and HC FreeSurfer surface labels to ROI masks in FSL anatomical T1 space using FreeSurfer's bbregister and mri_label2vol commands. Next, we registered V1, V2, and HC masks to DWI space using FSL FLIRT (FMRIB's Linear Image Registration Tool, Greve & Fischl, 2009; Jenkinson, Bannister, Brady, & Smith, 2002; Jenkinson & Smith, 2001) for probabilistic tractography (Figure 1, top, middle). V1 and V2 were merged into a single EVC ROI, as later fiber tracking from V1 and V2 were barely distinguishable (see 2.2.3 Diffusion weighed imaging).

2.2.2 Region of interest definition

To define scene-selective regions of interest (ROIs), we obtained functional MRI during a four-run scene localizer block design experiment that included scenes, objects, and a rest condition using a blood oxygen level dependent (BOLD) sensitive T2*-weighted sequence across 33 slices (TR = 2000 ms, TE = 30 ms, flip angle = 90°, FOV = 240 mm × 240 mm, voxel size = 3 mm × 3 mm × 3 mm, slice gap = 0.4 mm). Details of the scene localizer experimental design are reported elsewhere (Meissner et al., 2019b).

We used FSL FEAT (FMRIB's Software Library, version 5.0.11, RRID: SCR_002823,

Jenkinson, Beckmann, Behrens, Woolrich, & Smith, 2012; FMRI Expert Analysis Tool, version 6.0.0, Woolrich, Ripley, Brady, & Smith, 2001) for preprocessing and statistical analysis of functional MRI localizer data. Preprocessing of functional data included brain extraction, slice time correction, motion correction, high-pass temporal filtering (cutoff: 91 s) and registration to the T1 anatomical image for each run in a first-level analysis. First-level statistical results were then entered into a mixed-effects second-level analysis (FLAME 1 option; Woolrich, Behrens, Beckmann, Jenkinson, & Smith, 2004), yielding statistical *t*-value maps for the scene > object contrast for each participant.

To define ROIs, we registered each participant's *t*-value maps to her/his anatomical T1 image using sinc interpolation with FSL FLIRT (Figure 1, top, left). Using FSLeyes (version 0.22.6, McCarthy, 2018), we defined subject-specific PPA, RSC, and OPA in each hemisphere at plausible locations based on thresholded *t*-value maps (Figure 1, top, middle; for exemplary ROIs, see Figure 2a). For the PPA and RSC, we included contiguous voxels whose scenes > objects contrast exceeded the *t*-value of 5.75. For the OPA, we chose a more liberal threshold of $t > 4$, because the OPA can rarely be detected at the same threshold as the PPA and RSC (without overlapping and hardly

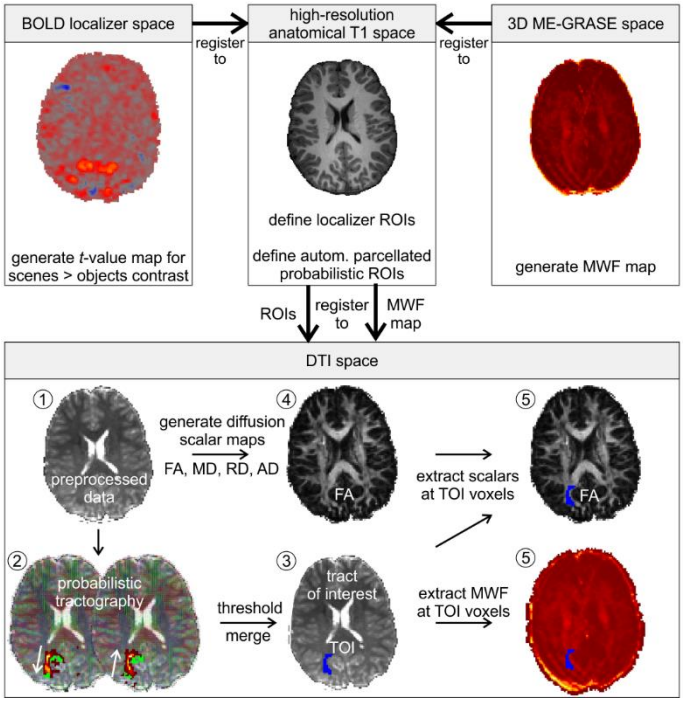

Figure 1: Analysis pipeline overview. The anatomical image in T1 space was used as a common intermediate registration template and connecting link between DTI space and non-diffusion spaces, i.e. BOLD and GRASE space. Numbers in circles indicate the order of analysis steps in DTI space. green = seed and target ROI (here: right RSC and OPA) for probabilistic tractography, heatmap arch = result for probabilistic tractography in which brighter colors indicate more samples crossing that voxel, blue = merged and thresholded TOI mask.

definably clusters of PPA and RSC at liberal thresholds or not detecting the OPA a conservative thresholds; cf. Meissner et al., 2019b).

For all ROIs, this approach yielded high detection rates that did not differ between age groups as determined using Fisher's exact test (S1 Table). One 11-12yo was excluded from subsequent analyses, because activations for the scenes > objects contrast did not exceed the set thresholds. For each participant, we registered the T1 anatomy to the b=0 DWI image using trilinear transformation with FSL FLIRT. The resulting transformation matrix was then used to register each ROI from anatomical T1 space to DWI space using nearest neighbor interpolation. For six ROIs in six participants, interpolation to the target space using the nearest neighbor algorithm failed. This was presumably due to their small size of 1 mm^3 to 5 mm^3 and the consequently difficult mapping to the quadrupled voxel size of 4 mm^3 of the DWI target space. To still include these ROIs in the analysis, we applied a trilinear interpolation approach in FSL FLIRT, which does not produce a binary mask, but a continuous probability map for that ROI in target space. To obtain a binary ROI mask again, we included all voxels at and above the probability map's median value. This procedure was successful for all six ROIs in which the original nearest neighbor algorithm failed.

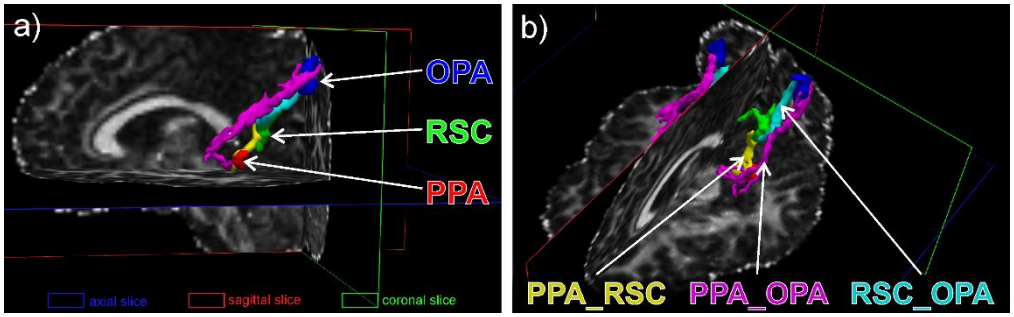

Figure 2: Scene-selective areas (a) and fiber tracts (b) for an exemplary 7-8yo participant. Areas and tracts are reconstructed in native 3D DTI space on top of a FA map. Areas, tracts, and FA map are smoothed for better visualization. Tracts are displayed in uniform color for easier identification; for an example of a tract probability (heat-)map, see Figure 1, bottom, left.

2.2.3 Diffusion weighted imaging

For fiber tracking and diffusion parameter analysis, a diffusion-weighted single-shot spin-echo EPI sequence along 33 isotropically distributed directions using a b-value of 1000 s/mm^2 (TR = 7234 ms, TE = 89 ms, flip angle = 90°, 60 slices, matrix size = 128 × 128, voxel size = 2 × 2 × 2 mm) was obtained. At the beginning of this sequence, one reference image was acquired without diffusion weighting (b = 0 s/mm^2). For analysis of diffusion weighted data, we used FSL's FDT (FMRIB's Diffusion Toolbox). Preprocessing of DWI data included eddy current and motion artefact correction

using FSL eddy_correct, diffusion gradient vectors reorientation to match the correction-induced rotations, as well as brain extraction (Figure 1, bottom, #1).

We performed probabilistic tractography on our data in native diffusion space using FSL BEDPOSTX and PROBTRACKX (Behrens et al., 2003; Behrens, Berg, Jbabdi, Rushworth, & Woolrich, 2007) with default settings, but 25,000 tract-following streamlines originating from each seed mask voxel (Figure 1, bottom, #2). For each participant, fiber tracking was done for 24 intrahemispheric tracts. In turn, each of the six scene-selective ROIs—as defined by our localizer (see 2.2.2, Region of interest definition)—was set as the seed mask. For each seed mask, i.e. for each scene-selective ROI, four ipsilateral target masks were set: 1-2) the two other scene ROIs, 3) the HC, 4) the EVC (Figure 3). For these 18 seed-target pairs, probabilistic tractography was done in both directions. That is, after the initial seed-to-target tracking was done, a target-to-seed tracking estimated the same tract in reverse direction (cf. Genç, Bergmann, Singer, & Kohler, 2011). For both directions, target masks were also set as waypoint and termination masks to ensure that only tracts would be retained that entered the target mask and that did not project onto other areas. Our rationale for employing this dual-direction approach was to control for any direction specific biases in probabilistic tractography, avoiding under- as well as overrepresentation of tract size or detectability. We refrained

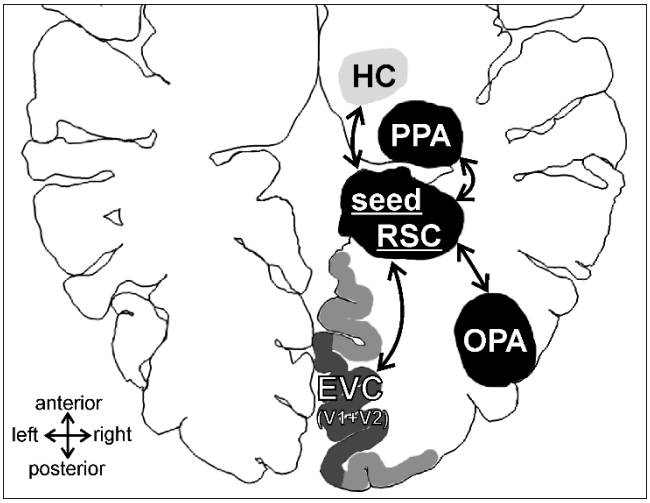

Figure 3: Schematic exemplary seed region (rRSC) with target regions and tract connections. For each scene-selective ROI, fiber tracking was done with the ipsilateral early visual cortex (EVC, i.e. a merged ROI of V1 and V2), hippocampus (HC), and the other two ipsilateral scene-selective ROIs (here: PPA and OPA). Note that in order to show all seed and target regions in one comprehensive display, this is a schematic drawing that does not reflect the appropriate absolute or relational position and size of target and seed regions.

from interhemispheric tracking, as DWI and MWI parameters from these tracts would be masked by a major share of general corpus callosum development adding little—if any—insight into scene-network specific development (for corpus callosum development, see Meissner et al., 2019a).

For each voxel, the resulting probability maps indicate how many of the streamlines that successfully connected seed-to-target crossed this voxel. However, these probability maps include low-probability voxels that are likely to be spurious connections. To remove these spurious connections, we threshold individual tract maps at 20% of their robust maximum (99th percentile) value (cf. Koldewyn et al., 2014) and then merged seed-to-target and target-to-seed tracts using a logical *and*-condition (Figure 1, bottom, #3; for exemplary tracts, see Figure 2b). Like other thresholding approaches, this accounts for systematically different ROI sizes. Moreover, in contrast to thresholding based on the number of initiated or successful streamlines, our approach provides a better interpretability, as the number of initiated or successful streamlines offers little insight into the actual probability map value distribution.

Originally, tracking from scene ROIs to the EVC was split into tracking to V1 and V2 based on their respective probabilistic FreeSurfer labels (see 2.2.1 High-resolution anatomical imaging and cortical parcellation). However, visual inspection of final thresholded tracts revealed that tracts from scene ROIs to V1 and V2 were overlapping for the most part. Thus, we merged V1 and V2 ROIs to an EVC ROI and repeated the tracking procedure for the EVC ROI.

To evaluate white matter microstructural integrity in fiber tracts of interest, we fit diffusion tensors, modelled by three pairs of eigenvectors ($\varepsilon_1, \varepsilon_2, \varepsilon_3$) and eigenvalues ($\lambda_1, \lambda_2, \lambda_3$) that describe the direction and magnitude of water diffusion along three orthogonal axes, to each voxel of our preprocessed DWI data using FSL DTIFIT. We then calculated axial, radial and mean diffusivity (AD = λ_1, RD = $(\lambda_1 + \lambda_2)/2$, MD = $(\lambda_1 + \lambda_2 + \lambda_3)/3$), as well as fractional anisotropy (FA = $\sqrt{3/2} \times \sqrt{(\lambda_1 - \mathrm{MD})^2 + (\lambda_2 - \mathrm{MD})^2 + (\lambda_3 - \mathrm{MD})^2} / \sqrt{\lambda_1^2 + \lambda_2^2 + \lambda_3^2}$) as diffusion parameters of interest (Figure 1, bottom, #4). Weighted mean diffusion tensor imaging (DTI) metric values for each tract were obtained that that considered each voxel's DTI metric values and tract probability (Yendiki et al., 2011, Figure 1, bottom, #5). In detail, the weighed mean is the sum of all tract voxels' DTI

metric values multiplied with their tract probabilities. Each voxel's tract probability is the crossing streamline count of the voxel divided by the sum of the crossing streamline count across all voxels.

2.2.4 Myelin water imaging

To examine the myelination state of white matter tracts, a 3D multi-echo (ME) gradient spin echo (GRASE) sequence with refocusing sweep angle was acquired (TR = 800 ms; TE = 10 - 320 ms, 32 echoes in steps of 10 ms, partial Fourier acquisition (z-direction: 50% overcontiguous slices, i.e. acquired slice thickness = 4 mm, reconstructed slice thickness =2 mm; y-direction: none), parallel imaging SENSE = 2.0, flip angle = 90°, 60 slices, matrix size = 112 × 112, voxel size = 2 × 2 × 2 mm, acquisition duration = 7.25 min). Parameter maps estimating the fraction of water molecules located between myelin layers—the myelin water fraction (MWF, MacKay et al., 1994)—for each voxel were created as described elsewhere (Prasloski et al., 2012). MWF maps were then registered to native DWI space using FSL FLIRT (Figure 1, top, right and middle). Here, for high-accuracy transformations, we employed a two-step procedure. First, we registered the TE = 10 ms image of the GRASE sequence to anatomical T1 space using trilinear transformation. The resulting transformation matrix was then used to register the MWF map to anatomical T1 space using sinc interpolation. Second, we registered the T1 anatomy to the b=0 DWI image using trilinear transformation. The resulting transformation matrix was then used to register the MWF map from anatomical T1 space to DWI space using sinc interpolation. Weighted mean MWF values for each tract were obtained that considered each voxel's MWF value and tract probability (in the same way as it was done for DWI, Figure 1, bottom, #5).

2.3 Neuroimaging data quality control

We screened preprocessed 4D DWI data and FA maps for visible artefacts that were not corrected by the preprocessing steps and excluded one 7-8yo participant from subsequent analyses. Further, to control for possible age group differences in DWI data quality, we quantified two registration-based and two intensity-based data quality measures implemented in the FreeSurfer TRACULA toolbox (Yendiki et al., 2011). For the registration-based measures, mean volume-to-volume translation and rotation parameters were obtained from affine registration matrices of each volume to the first (b=0) volume. This was to capture global, slow between-volume motion. Our analysis of variance (ANOVA) on both translation and rotation parameters did not reveal any

significant between-group differences (Figure 4; rotation: $F(2,44) = 1.52$, $p = .230$, $\eta^2 = .065$ translation: $F(2,44) = 2.27$, $p = .115$, $\eta^2 = .094$)

For the intensity-based measures, we calculated a signal intensity drop-out score for each slice in each volume in reference to the corresponding slice in the b=0 volume as proposed by Benner et al. (2011). This was to capture the effect of rapid within-volume motion (note: TR = 7234 ms). We then

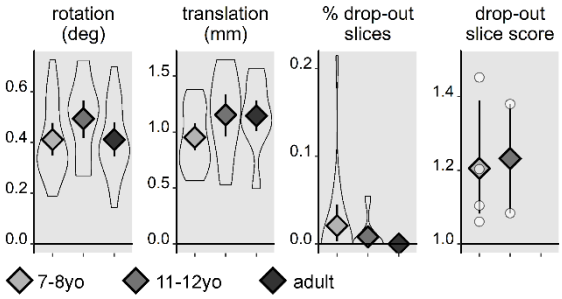

Figure 4: Between-group data quality comparison after matching for the percentage of drop-out slices. Gray diamonds = group mean. Light gray = 7-8-year-old children, medium gray = 11-12-year-old children, dark gray = adults. Violin plots show the full distribution of the data. White circles = individual data points. Error bars show 95% confidence intervals for the mean.

quantified the percentage of slices with suspect signal drop-out across the scan—indicated by a score greater than 1—as well as the average signal drop-out severity for those "bad" slices. Four 7-8yo, two 11-12yo, but no adults displayed any slices with strong signal dropout (Figure 4). In participants with signal dropout, we observed a maximum portion for "bad" slices of 0.21 %. Due to the low number of participants with signal dropout, and no signal dropout in the adult group (i.e. no variance) any ANOVA-based group comparison for the drop-out slice score or percentage of drop-out slices would lack validity. Thus, we employed Fisher's exact test and found that the number of participants with any signal-dropout did not differ between age groups ($\chi^2(2) = 3.87$, $p = .152$).

As the 3D signal acquisition method of the GRASE sequence is not volume-based, affine registration matrices and corresponding motion estimates, like for functional MRI or DWI cannot be computed for 3D ME-GRASE data. However, we visually screened all raw GRASE images as well as MWF maps for motion artefacts but found none.

2.4 Experimental design, statistical analysis

Our study investigated the effect of the between-subject factor age group (with three levels) on the outcome variables MWF, FA, MD, RD, and AD for six scene-selective fiber tracts. In an

exploratory analysis, further tracts were tested between all six scene-selective ROIs and the EVC and HC, respectively. To test for differences between age groups, we employed analysis of variances (ANOVAs) for each fiber tract independently. To correct for multiple comparison, the default significance threshold of $\alpha = .05$ was Bonferroni-corrected for 6 tracts to $\alpha = .0083$. To improve the usability of our results for colleagues whose research interest focuses on one or a particular region or tract of interest only, we also report age group effects that reached the uncorrected significance threshold of $\alpha = .05$ in a second step. Statistical data analysis was performed using R (version 3.6.0, RRID: SCR_001905, R Core Team, 2019) in RStudio (version 1.2.1335; RRID: SCR_000432).

3 Results

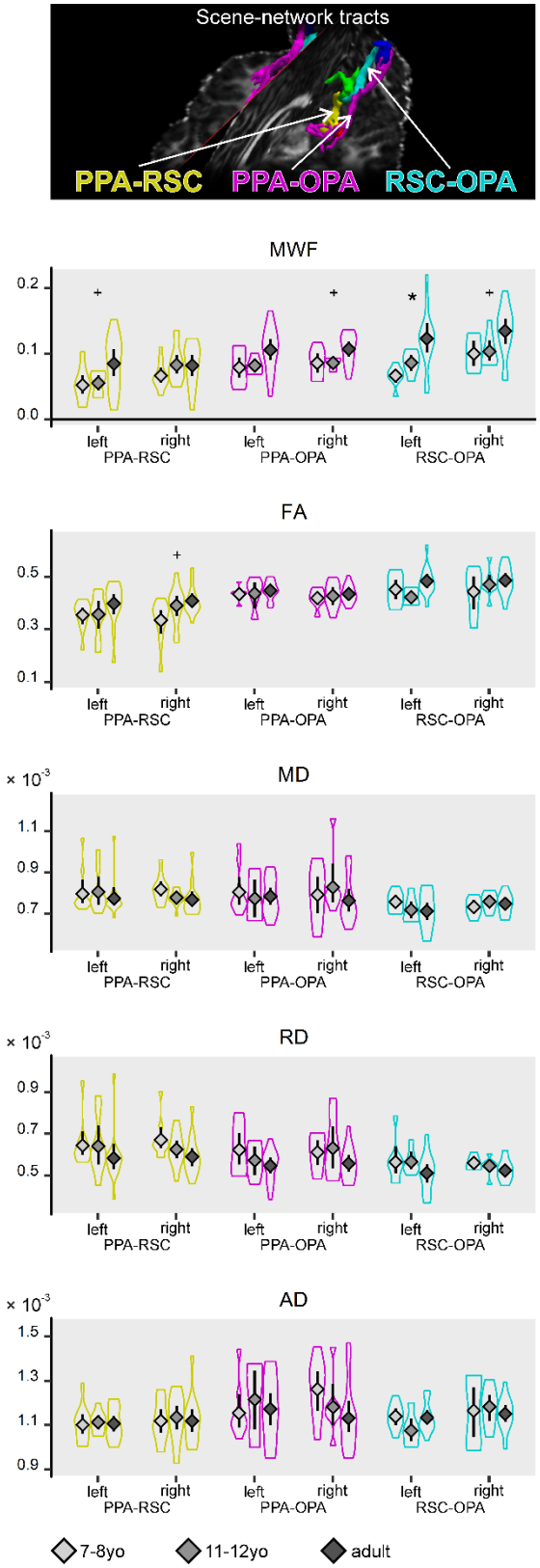

Figure 5: Myelin water fraction (MWF) and DTI parameters for intrahemispheric connections between scene-network areas. Gray diamonds = group mean. Light gray = 7-8-year-old children, medium gray = 11-12-year-old children, dark gray = adults. Error bars show 95% confidence intervals for the mean. Violin plots show the full distribution of the data. Asterisks and plus signs indicate significance with Bonferroni correction (α = .0083) and without correction for multiple comparisons (α = .05), respectively.

337 This study combined myelin water imaging with a functional MRI scene localizer and DWI-
338 based tractography to determine the degree of myelination in white matter tracts underlying the
339 cortical scene-network in three age groups. We examined possible differences in myelin water fraction
340 between eighteen 7-8yo, thirteen 11-12yo, and sixteen adults to examine if the scene-network's white
341 matter structural connectivity follows a similar or divergent pattern in reference to scene-network's
342 functional development. Further, we investigated connections between the scene-network and key
343 input areas, such as EVC and the HC. In an extended analysis, we tested whether DTI parameters
344 showed the same pattern as MWF.

345 ## 3.1 Myelin water imaging

346 Regarding within-scene-network tracts, the MWF in fibers connecting the left RSC and OPA
347 increased with age ($F(2,25) = 7.40$, $p = .0030$, $\eta^2 = .372$, Figure 5). We observed further increases,
348 albeit not surviving Bonferroni correction, for the right RSC-OPA tract ($F(2,25) = 3.47$, $p = .0470$, η^2
349 $= .217$), the left PPA-RSC tract ($F(2,31) = 3.99$, $p = .0288$, $\eta^2 = .205$), and the right PPA-OPA tract
350 ($F(2,26) = 3.82$, $p = .0352$, $\eta^2 = .227$).

351 For connections between the HC and scene-network areas, we found increasing MWF with
352 age in tracts connecting to the OPA in both hemispheres (left: $F(2,36) = 8.20$, $p = .0012$, $\eta^2 = .313$;
353 right: $F(2,37) = 5.97$, $p = .0056$, $\eta^2 = .244$, Figure 6, first row left).

354 EVC-scene-network connections showed no significant increasing MWF with age. Non-
355 significant increases, i.e. not surviving Bonferroni-correction, were observed for the left RSC-EVC
356 tract ($F(2,39) = 3.76$, $p = .0320$, $\eta^2 = .162$) and for OPA-EVC tracts in both hemispheres (left: $F(2,36)$
357 $= 5.18$, $p = .0105$, $\eta^2 = .224$; right: $F(2,37) = 5.18$, $p = .0104$, $\eta^2 = .219$, Figure 6, first row right).

358 ## 3.2 Extended analysis of DTI parameters

359 Regarding within-scene-network tracts, the age group differences observed for MWF was not
360 mirrored in DTI parameters. For FA, we found increasing MWF with age in the right PPARSC tract,
361 but statistical significance did not meet our Bonferroni-correction criterion ($F(2,36) = 3.80$, $p = .0318$,
362 $\eta^2 = .174$, Figure 5, second row). No other tract showed age effects for FA. Concerning the other DTI

parameters—MD, RD, and AD—we did not find any tracts with age group differences (Figure 5, third, fourth, and fifth row).

HC-scene-network connections showed the same pattern for FA as for MWF. Tracts from the HC to the left and right OPA showed increasing FA with age (left: $F(2,36) = 6.73$, $p = .0033$, $\eta^2 = .272$; right: $F(2,37) = 11.86$, $p = .0001$, $\eta^2 = .391$, Figure 6, left, second row). However, other DTI parameters did not mirror MWF findings: MD showed an increase in left lPPA-HC connections with age ($F(2,41) = 6.24$, $p = .0043$, $\eta^2 = .233$, Figure 6, third row left), but not in other tracts. RD did not reveal differences between age groups in HC-connecting tracts. Concerning AD, tracts connecting the PPA and the HC showed age group differences, albeit increasing values for the left and decreasing values for the right hemisphere and not surviving Bonferroni-correction in either hemisphere (left: $F(2,41) = 4.14$, $p = .0230$, $\eta^2 = .168$; right: $F(2,41) = 3.40$, $p = .0431$, $\eta^2 = .142$, Figure 6, last row left).

In EVC-scene-network connections, DTI parameters did not exhibit age group differences that survived Bonferroni correction (Figure 6, second to fifth row, right). Only uncorrected, i.e. non-significant effects were found for decreasing RD in the left PPA-EVC tract ($F(2,41) = 4.25$, $p = .0210$, $\eta^2 = .172$) and the right OPA-EVC tract ($F(2,37) = 3.33$, $p = .0467$, $\eta^2 = .153$, Figure 6, fourth row right).

3.3 Control analyses

To control for the possibility that any of the observed age effects were confounded by age-related tract volume differences, we compared tract volume between age groups using ANOVAs and found differences in tracts from the left PPA to the HC and EVC, from the right PPA to the HC and from the right OPA to the HC, but not in any other tracts (lPPA-HC: $F(2,41) = 7.01$, $p = .0024$, $\eta^2 = .254$; lPPA-EVC: $F(2,41) = 6.18$, $p = .0045$, $\eta^2 = .232$; rPPA-HC: $F(2,41) = 7.89$, $p = .0013$, $\eta^2 = .278$; rOPA-HC: $F(2,37) = 6.85$, $p = .0029$, $\eta^2 = .270$). Thus, while MD effects in lPPA-HC tracts, RD

387 effects in lPPA-EVC tracts, as well as FA and MWF effects in rOPA-HC tracts might stem from tract

388 size differences between age groups, for all other tracts, volume seems an unlikely bias.

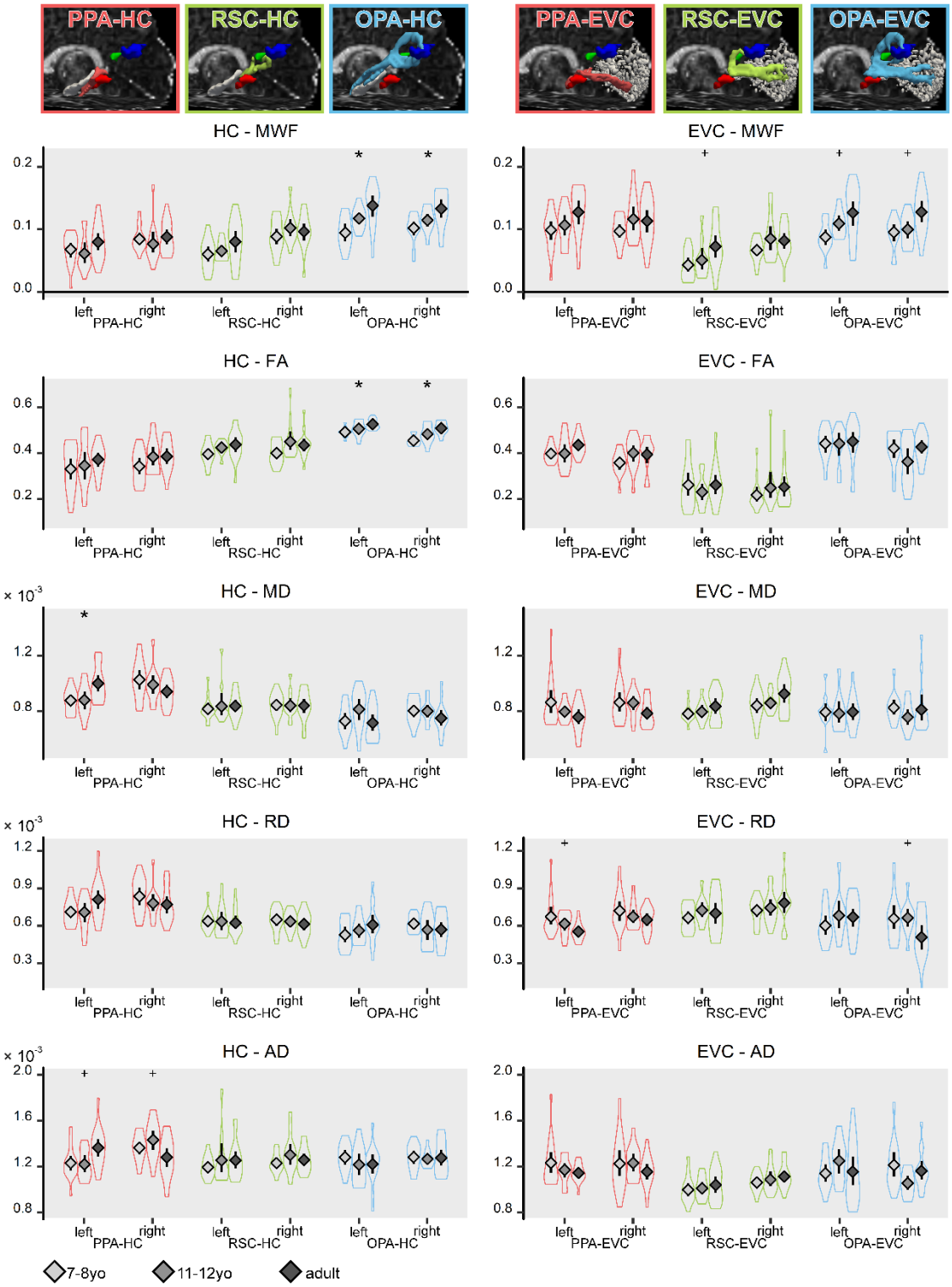

Figure 6: Myelin water fraction (MWF) and DTI parameters for connections between scene-network areas and the hippocampus (HC, left), early visual cortex (EVC, right). Gray diamonds = group mean. Light gray = 7-8-year-old children, medium gray = 11-12-year-old children, dark gray = adults. Error bars show 95% confidence intervals for the mean. Violin plots show the full distribution of the data. Asterisks and plus signs indicate significance with Bonferroni correction (α = .0083) and without correction for multiple comparisons (α = .05), respectively

389

4 Discussion

Myelin emergence and further maturation is a crucial step in brain development (Flechsig, 1920). While myelin development trajectories for white matter beyond late childhood are still unclear, it is established that the rate of change and the point at which an adult level is reached is region specific (Yakovlev & Lecours, 1967). Further, myelin maturation was shown to interact with functional organization and behavior (e.g. Bengtsson et al., 2005; Yeatman, Dougherty, Ben-Shachar, & Wandell, 2012). Here, we compared MWF in white matter tracts underlying the visual scene-network between 7-8yo, 11-12yo and adults. We found increasing MWF in the left RSC-OPA tract and non-significant trends for increasing MWF in the right RSC-OPA, left PPA-RSC, and right PPA-OPA tracts. Moreover, myelin increased in connections from the left and right OPA to the HC, which is strongly involved in scene-processing. Moreover, myelin showed non-significant trends to increase in connections of the left and right OPA and the left RSC with the EVC, which is a major input area for scene-selective cortex.

4.1 Connections between scene network areas

Our findings provide evidence for a protracted development of white matter tracts that connect the scene-network regions PPA, RSC, and OPA. While age effects were only significant after Bonferroni correction in the left RSC-OPA tract, effect sizes for the non-significant trends right RSC-OPA, left PPA-RSC, and right PPA-OPA tracts were medium-to-large. Thus, we hope that future higher-powered work with larger sample sizes will confirm these trends. The two tracts that did not even pass the $\alpha = .05$ significance threshold show increasing mean MWF with age on a descriptive level. Altogether, these findings suggest a myelin increase in scene network tracts with specific tracts displaying more pronounced age effects than others.

This pattern would suggest that scene network tracts' developmental trajectory resembles that of major long white matter tracts. Recent findings indicate that myelin in a majority of major white matter tracts increases from childhood into young adulthood (Meissner et al., 2019a). In this study, major tracts that may partly subserve scene network connecting tracts—i.e. the inferior longitudinal fasciculus—showed moderate myelin increases from middle childhood to adulthood. However, this

remains speculative until other studies can replicate these findings, as our study's population was equal to the one investigated in Meissner et al. (2019a). If confirmed, this pattern would suggest a resemblance to cortical gray matter myelin content development, which displays development across late adolescence and up to early adulthood, too (Carey et al., 2018; Grydeland, Walhovd, Tamnes, Westlye, & Fjell, 2013; Miller et al., 2012; Shafee, Buckner, & Fischl, 2015).

Integrating our results with recent findings of functional cortical development in scene-selective areas during and beyond childhood (Chai et al., 2010; Golarai et al., 2007; Meissner et al., 2019b) opens up the possibility of structure-function interactions, i.e. influences of structural development on functional development, or vice versa. However, while previous studies established that the RSC is adult-like in middle childhood already (Jiang et al., 2014; Meissner et al., 2019b), tracts connecting the RSC to the left OPA (and possibly to the right OPA and left PPA) displayed development nonetheless. Either, this could mean that if structure-function interactions exist, they do not need the involvement, i.e. development, of both cortical ends of a tract. Or, no interactions might exist, i.e. structural and functional development might be independent. As cortical structure, function, and associated cognitive abilities have been associated with white matter structural development (Fields, 2008; Gomez et al., 2017), we speculate that a completely independent development of structure and function is unlikely.

4.2 Connections between the scene network, hippocampus, and EVC

Connections from the OPA to the HC indicate increasing myelination from middle childhood to adulthood in both hemispheres. For OPA-EVC connections, non-significant trends towards a myelin increase were observed. Interestingly, functional cluster size as well as scene selectivity in bilateral OPA was shown to increase along the same trajectory (Meissner et al., 2019b). As for within-scene network connections, to speculate, functional OPA development could be driven by maturing connections to input/output areas. Or, vice, versa, the maturation of OPA-associated fibers could be a case of activity dependent myelination (Fields, 2008). Connections from left RSC to EVC showed moderate effect sizes but significance did not survive Bonferroni correction. Possibly, this trend is a residual of an activity-dependent myelination that started following the completion of functional RSC maturation.

4.3 Diffusion tensor imaging interpretation

None of the investigated DTI parameters (FA, MD, RD, AD) mirrored any MWI findings except for FA age effects in connections between the scene network and the HC, where FA increased with age in left and right OPA-HC tracts. This generally missing correspondence might be explained by the fact that fiber geometry has a particularly high influence on DTI parameters in small tracts—like connections between scene-network areas. This high influence is due to a higher probability that two tracts with diverging principal diffusion directions cross, branch, or merge within one voxel (Feldman et al., 2010). Thus, especially in small tracts, the use of DTI parameters as a proxy for myelin is problematic and might not reflect myelination but rather other microstructural changes (Moura et al., 2016). For example, a recent study on the same study population that investigated major large tracts found a comparatively higher correspondence between DTI and MWF effects (Meissner et al., 2019a).

4.4 Limitations

With our investigation on the scene network white matter development our study provides an important contribution to an integrated understanding of how the scene network of PPA, RSC, and OPA develops. However, the methodological approach of our study has certain limitations that are discussed below.

Previous studies indicate that the optimal ratio of low-b acquisitions and high-b acquisitions is 0.1 (Jones, Horsfield, & Simmons, 1999) to 0.2 (Alexander & Barker, 2005). Consequently, an optimal ratio for our protocol of 33 high-b acquisitions, would be achieved with 3-6 low-b (b=0) acquisitions (Mukherjee, Chung, Berman, Hess, & Henry, 2008). However, software limitations (Mukherjee et al., 2008) at the time of the recordings prevented the acquisition of more than one b=0 for a DWI session. Future studies with optimal scan protocols should therefore test whether our results are replicable.

The majority of studies in cognitive and developmental cognitive neuroscience quantify fiber geometry and microstructural properties of fiber tracts by means of the tensor model. This model assumes that, in each voxel, there is a unique orientation of fibers, the direction of which is represented by the tensor's main eigenvector (Mori & Tournier, 2014). However, large portions of

white matter voxels contain multiple fiber orientations (Jeurissen, Leemans, Tournier, Jones, & Sijbers, 2013). Therefore, tensor models are naturally limited to deal with voxels containing multiple fiber orientations (e.g. crossing fibers). Non-tensor-based models such as the method of constrained spherical deconvolution (CSD, Tournier, Calamante, Gadian, & Connelly, 2004) can be used to estimate the distribution of fiber orientations present within each voxel. With this method, the signal is measured by means of a high angular resolution diffusion imaging (HARDI) session, which should contain at least 45 diffusion directions (Tournier, Calamante, & Connelly, 2009) and higher b-values (e.g. b=3000, Farquharson et al., 2013). The diffusion signal measured with such a scan protocol can be expressed as the convolution—over spherical coordinates—of the response function representing the signal of a single coherently oriented population of fibers, with the fiber orientation distribution. In general, these kinds of deconvolution methods lead to a robust determination of the fiber orientations in voxel within a clinically acceptable time (Farquharson et al., 2013; Mori & Tournier, 2014) and have been shown to be superior to DWI-based tractography in the context of neurosurgical planning (Farquharson et al., 2013). With 33 diffusion directions and b-values of 1000 our scan protocol is not optimized for these kinds of advanced methods, so future should test whether the development of scene network-specific white matter tracts show similar trajectories if CSD-fiber tracking is employed.

As stated above, large portions of white matter voxels contain multiple fiber orientations (Jeurissen et al., 2013). While MWF is more specific to myelin than DTI-derived parameters, it is still not clear which exact axons within a voxel contribute to the MWF. Pathways that overlap and cross our scene-specific pathways in a substantially different direction, i.e. axon populations within voxels of our scene-pathways that do not serve the scene-specific connection, could influence the MWF at these points. Upon visual inspection, we could not identify major pathways that cross the scene-specific pathways on a regular basis except for the superior longitudinal fasciculus (SLF) that crosses the PPA-OPA tract. Aside from the fact that only for 1/6 of the tracts, a potential crossing tract exists that is reliably and automatically traceable with our data, even for the SLF and the PPA-OPA tract, the actual overlap was minimal: Only four tracts in four participants showed an overlap of more than 10% shared voxels and the maximum overlap was 18.9% shared voxels. Thus, the possible bias or the

possibility to identify a bias by quantifying MWF in cross-over and non-cross-over voxels is very small.

MWF has shown strong qualitative and quantitative correspondence with histological markers for myelin (Laule et al., 2006; Laule et al., 2008). Still, it is important to be aware of potential confounding factors that may influence in vivo measurement of myelin water—which remains an indirect measure (MacKay & Laule, 2016). The most important factor is movement of water from myelin bilayers during the measurement. The T2 decay curve approach, which is used for the MWF, assumes that water molecules stay in the myelin bilayers for long times compared to the decay curve measurement time. However, at least studies in rodent spines indicate that during the measurement water molecules might be able to move from myelin in sufficiently fast rates to cause artificially low MWF (Harkins, Dula, & Does, 2012; Levesque & Pike, 2009). At the same time, other studies in animals indicate that water exchange does not play a considerable role in MWF measurements (Stanisz, Kecojevic, Bronskill, & Henkelman, 1999). The effect of water exchange in humans has not yet been accurately quantified; however, it seems likely that measured MWF are slight underestimates of the true MWF (Kalantari, Laule, Bjarnason, Vavasour, & MacKay, 2011). Moreover, future studies should compare our findings to alternative in vivo MRI measures that are able to quantify myelin architecture, such as magnetization transfer imaging (MacKay & Laule, 2016), bound pool fraction (Stikov et al., 2011), or myelin density (Sepehrband et al., 2015).

4.5 Outlook

Here, we investigated the development of myelin in white matter tracts subserving the cortical visual scene network for the first time. We established that myelin seems to increase in several within-scene network tracts as well as in connections to crucial input regions. These results are exciting in so far as they demonstrate that the protracted scene network development between childhood and adulthood is not limited to functional changes, but also includes maturation of underlying structures that are not directly part of the cortical network. We are positive that our study opens up two further directions going forward. First, our cross-sectional study paves the way for large-scale longitudinal studies with short time intervals over an extended period of time and a high number of participants that combine behavioral testing, fMRI, DWI-tractography, and MWI, which could tap into the

528 important question of structure-function-development in more detail. Second, next to the scene
529 network, other cortical category-specific high-level vision areas form networks. For example, face
530 processing is supported by a core network with modules in the fusiform gyrus, inferior occipital gyrus,
531 and superior temporal sulcus, for which evidence also suggests a prolonged functional development
532 (e.g. Golarai et al., 2007; Nordt, Semmelmann, Genç, & Weigelt, 2018, for a review see Haist &
533 Anzures, 2017). Only little evidence, based on DTI analysis of major white matter tracts, exists that
534 hints at possible emerging structure-function relations in the developing face processing system
535 (Scherf, Thomas, Doyle, & Behrmann, 2014). Using MWI and tractography of individual, short-range,
536 face-area-specific tracts, future research might corroborate these first findings and shed more light on
537 structural white matter development as a contributing developmental factor on the long way to (face)
538 perception expertise.

Acknowledgements

We thank our team of student assistants and interns for assisting in stimulus creation, pilot testing, subject recruiting, and data collection. We acknowledge the support of the Neuroimaging Centre of the Research Department of Neuroscience at Ruhr University Bochum's teaching hospital Bergmannsheil and Philips GmbH, Germany. We thank all participants and their parents for participating in this study.

Funding

This work was supported by a PhD scholarship of the Konrad-Adenauer-Foundation and an International Realization Budget of the Ruhr University Bochum Research School PLUS through funds of the German Research Foundation's Universities Excellence Initiative (GSC 98/3) to TWM, grants from the German Research Foundation (GE 2777/2-1 and SFB 1280 project A03), the Mercator Research Center Ruhr (AN-2015-0044) to EG, and grants from the Deutsche Forschungsgemeinschaft (DFG, German Research Foundation, project number WE 5802/1-1 and project number 316803389 – SFB 1280 project A16), the Mercator Research Center Ruhr (AN-2014-0056), and the Volkswagen Foundation (Lichtenberg Professorship, 97 079) to SW.

Data and code availability statement

All code used for data analysis (except for the MWF parameter map generating algorithm, which is available upon request), as well as anonymized raw data are publicly available at the Open Science Framework (https://doi.org/10.17605/osf.io/dbg83).

Ethics statement

The Ruhr University Bochum Faculty of Psychology ethics board approved the study (proposal no. 280). All participants as well as children's parents gave informed written consent to participate voluntarily.

Conflict of interest statement

BM works at Philips GmbH, Hamburg, Germany. Philips is the manufacturer and support service provider for the MRI machine used in this study. BM developed and implemented the GRASE sequence at the scanner and co-developed and provided the MWF maps generating algorithm. BM and Philips GmbH had no role in the funding, conceptualization, design, or statistical analysis of the study.

Author contributions

Conceptualization: TWM, SW; Methodology: EG, BM; Software: BM; Formal Analysis: TWM, EG; Investigation: TWM; Resources: SW, EG; Data Curation: TWM; Writing—Original Draft: TWM; Writing—Review and Editing: TWM, SW, EG, BM; Visualization: TWM; Supervision: SW, EG; Project Administration: TWM; Funding Acquisition: SW, TWM

References

Alexander, D. C., & Barker, G. J. (2005). Optimal imaging parameters for fiber-orientation estimation in diffusion MRI. *Neuroimage*, *27*(2), 357–367.

Baldassano, C., Beck, D. M., & Fei-Fei, L. (2013). Differential connectivity within the Parahippocampal Place Area. *Neuroimage*, *75*, 228–237.

Baldassano, C., Esteva, A., Fei-Fei, L., & Beck, D. M. (2016a). Two Distinct Scene-Processing Networks Connecting Vision and Memory. *eNeuro*, *3*(5).

Baldassano, C., Fei-Fei, L., & Beck, D. M. (2016b). Pinpointing the peripheral bias in neural scene-processing networks during natural viewing. *Journal of vision*, *16*(2), 9.

Barnea-Goraly, N., Menon, V., Eckert, M., Tamm, L., Bammer, R., Karchemskiy, A., et al. (2005). White matter development during childhood and adolescence: a cross-sectional diffusion tensor imaging study. *Cerebral Cortex*, *15*(12), 1848–1854.

Behrens, T. E. J., Berg, H. J., Jbabdi, S., Rushworth, M. F. S., & Woolrich, M. W. (2007). Probabilistic diffusion tractography with multiple fibre orientations: What can we gain? *Neuroimage*, *34*(1), 144–155.

Behrens, T. E. J., Woolrich, M. W., Jenkinson, M., Johansen-Berg, H., Nunes, R. G., Clare, S., et al. (2003). Characterization and propagation of uncertainty in diffusion-weighted MR imaging. *Magnetic resonance in medicine*, *50*(5), 1077–1088.

Bengtsson, S. L., Nagy, Z., Skare, S., Forsman, L., Forssberg, H., & Ullén, F. (2005). Extensive piano practicing has regionally specific effects on white matter development. *Nature neuroscience*, *8*(9), 1148–1150.

Benner, T., van der Kouwe, A. J. W., & Sorensen, A. G. (2011). Diffusion imaging with prospective motion correction and reacquisition. *Magnetic resonance in medicine*, *66*(1), 154–167.

Bettencourt, K. C., & Xu, Y. (2013). The role of transverse occipital sulcus in scene perception and its relationship to object individuation in inferior intraparietal sulcus. *Journal of cognitive neuroscience*, *25*(10), 1711–1722.

600 Carey, D., Caprini, F., Allen, M., Lutti, A., Weiskopf, N., Rees, G., et al. (2018). Quantitative MRI
601 provides markers of intra-, inter-regional, and age-related differences in young adult cortical
602 microstructure. *Neuroimage*, *182*, 429–440.

603 Chai, X. J., Ofen, N., Jacobs, L. F., & Gabrieli, J. D.E. (2010). Scene complexity: Influence on
604 perception, memory, and development in the medial temporal lobe. *Frontiers in Human*
605 *Neuroscience*, *4*(21), 21.

606 Dale, A. M., Fischl, B., & Sereno, M. I. (1999). Cortical surface-based analysis. I. Segmentation and
607 surface reconstruction. *Neuroimage*, *9*(2), 179–194.

608 Dalton, M. A., Zeidman, P., McCormick, C., & Maguire, E. A. (2018). Differentiable Processing of
609 Objects, Associations, and Scenes within the Hippocampus. *The Journal of Neuroscience*, *38*(38),
610 8146–8159.

611 Day, M. C. (1975). Developmental Trends in Visual Scanning. In Hayne Reese (Ed.), *Advances in*
612 *Child Development and Behavior* (1st ed., pp. 153–193). Cambridge, MA: Academic Press.

613 Dean, D. C., O'Muircheartaigh, J., Dirks, H., Waskiewicz, N., Lehman, K., Walker, L., et al. (2014).
614 Modeling healthy male white matter and myelin development: 3 through 60months of age.
615 *Neuroimage*, *84*, 742–752.

616 Dean, D. C., O'Muircheartaigh, J., Dirks, H., Waskiewicz, N., Walker, L., Doernberg, E., et al. (2015).
617 Characterizing longitudinal white matter development during early childhood. *Brain structure &*
618 *function*, *220*(4), 1921–1933.

619 Deoni, S. C. L., Dean, D. C., O'Muircheartaigh, J., Dirks, H., & Jerskey, B. A. (2012). Investigating
620 white matter development in infancy and early childhood using myelin water faction and relaxation
621 time mapping. *Neuroimage*, *63*(3), 1038–1053.

622 Deoni, S. C. L., Dean, D. C., Remer, J., Dirks, H., & O'Muircheartaigh, J. (2015). Cortical maturation
623 and myelination in healthy toddlers and young children. *Neuroimage*, *115*, 147–161.

624 Deoni, S. C. L., Mercure, E., Blasi, A., Gasston, D., Thomson, A., Johnson, M., et al. (2011). Mapping
625 infant brain myelination with magnetic resonance imaging. *The Journal of Neuroscience*, *31*(2),
626 784–791.

627 Deoni, S. C. L., Rutt, B. K., Arun, T., Pierpaoli, C., & Jones, D. K. (2008). Gleaning multicomponent
628 T1 and T2 information from steady-state imaging data. *Magnetic resonance in medicine*, *60*(6),
629 1372–1387.

630 Dilks, D. D., Julian, J. B., Kubilius, J., Spelke, E. S., & Kanwisher, N. (2011). Mirror-image
631 sensitivity and invariance in object and scene processing pathways. *The Journal of Neuroscience*,
632 *31*(31), 11305–11312.

633 Epstein, R. A. (2008). Parahippocampal and retrosplenial contributions to human spatial navigation.
634 *Trends in cognitive sciences*, *12*(10), 388–396.

635 Epstein, R. A., & Baker, C. I. (2019). Scene Perception in the Human Brain. *Annual review of vision*
636 *science*, *5*, 373–397.

637 Epstein, R. A., & Higgins, J. S. (2007). Differential parahippocampal and retrosplenial involvement in
638 three types of visual scene recognition. *Cerebral Cortex*, *17*(7), 1680–1693.

639 Epstein, R. A., Higgins, J. S., Jablonski, K., & Feiler, A. M. (2007a). Visual scene processing in
640 familiar and unfamiliar environments. *Journal of neurophysiology*, *97*(5), 3670–3683.

641 Epstein, R. A., & Kanwisher, N. (1998). A cortical representation of the local visual environment.
642 *Nature*, *392*(6676), 598–601.

643 Epstein, R. A., Parker, W. E., & Feiler, A. M. (2007b). Where am I now? Distinct roles for
644 parahippocampal and retrosplenial cortices in place recognition. *The Journal of Neuroscience*,
645 *27*(23), 6141–6149.

646 Farquharson, S., Tournier, J.-D., Calamante, F., Fabinyi, G., Schneider-Kolsky, M., Jackson, G. D., &
647 Connelly, A. (2013). White matter fiber tractography: why we need to move beyond DTI. *Journal*
648 *of neurosurgery*, *118*(6), 1367–1377.

649 Feldman, H. M., Yeatman, J. D., Lee, E. S., Barde, L. H. F., & Gaman-Bean, S. (2010). Diffusion
650 tensor imaging: a review for pediatric researchers and clinicians. *Journal of developmental and*
651 *behavioral pediatrics*, *31*(4), 346–356.

652 Fields, R. D. (2008). White matter in learning, cognition and psychiatric disorders. *Trends in*
653 *Neurosciences*, *31*(7), 361–370.

654 Fields, R. D. (2015). A new mechanism of nervous system plasticity: activity-dependent myelination.
655 *Nature Reviews Neuroscience*, *16*(12), 756–767.

656 Fischl, B., Rajendran, N., Busa, E., Augustinack, J., Hinds, O., Yeo, B. T. T., et al. (2008). Cortical
657 folding patterns and predicting cytoarchitecture. *Cerebral Cortex*, *18*(8), 1973–1980.

658 Fischl, B., Salat, D. H., Busa, E., Albert, M., Dieterich, M., Haselgrove, C., et al. (2002). Whole Brain
659 Segmentation. *Neuron*, *33*(3), 341–355.

660 Fischl, B., Sereno, M. I., & Dale, A. M. (1999). Cortical surface-based analysis. II: Inflation,
661 flattening, and a surface-based coordinate system. *Neuroimage*, *9*(2), 195–207.

662 Fischl, B., van der Kouwe, A., Destrieux, C., Halgren, E., Ségonne, F., Salat, D. H., et al. (2004).
663 Automatically parcellating the human cerebral cortex. *Cerebral Cortex*, *14*(1), 11–22.

664 Flechsig, P. (1920). *Anatomie des menschlichen Gehirns und Rückenmarks auf myelogenetischer*
665 *Grundlage*. Leipzig: Thieme.

666 Ford, J. C., Hackney, D. B., Lavi, E., Phillips, M., & Patel, U. (1998). Dependence of apparent
667 diffusion coefficients on axonal spacing, membrane permeability, and diffusion time in spinal cord
668 white matter. *Journal of magnetic resonance imaging*, *8*(4), 775–782.

669 Geeraert, B. L., Lebel, R. M., Mah, A. C., Deoni, S. C. L., Alsop, D. C., Varma, G., & Lebel, C.
670 (2018). A comparison of inhomogeneous magnetization transfer, myelin volume fraction, and
671 diffusion tensor imaging measures in healthy children. *Neuroimage*, *182*, 343–350.

672 Genç, E., Bergmann, J., Singer, W., & Kohler, A. (2011). Interhemispheric connections shape
673 subjective experience of bistable motion. *Current Biology*, *21*(17), 1494–1499.

674 Ghosh, S. S., Kakunoori, S., Augustinack, J., Nieto-Castanon, A., Kovelman, I., Gaab, N., et al.
675 (2010). Evaluating the validity of volume-based and surface-based brain image registration for
676 developmental cognitive neuroscience studies in children 4 to 11 years of age. *Neuroimage*, *53*(1),
677 85–93.

678 Golarai, G., Ghahremani, D. G., Whitfield-Gabrieli, S., Reiss, A., Eberhardt, J. L., Gabrieli, J. D.E., &
679 Grill-Spector, K. (2007). Differential development of high-level visual cortex correlates with
680 category-specific recognition memory. *Nature neuroscience*, *10*(4), 512–522.

681 Gomez, J., Barnett, M. A., Natu, V., Mezer, A., Palomero-Gallagher, N., Weiner, K. S., et al. (2017).
682 Microstructural proliferation in human cortex is coupled with the development of face processing.
683 *Science*, *355*(6320), 68–71.

684 Graham, K. S., Barense, M. D., & Lee, A. C. H. (2010). Going beyond LTM in the MTL: a synthesis
685 of neuropsychological and neuroimaging findings on the role of the medial temporal lobe in
686 memory and perception. *Neuropsychologia*, *48*(4), 831–853.

687 Greve, D. N., & Fischl, B. (2009). Accurate and robust brain image alignment using boundary-based
688 registration. *Neuroimage*, *48*(1), 63–72.

689 Grill-Spector, K. (2003). The neural basis of object perception. *Current Opinion in Neurobiology*,
690 *13*(2), 159–166.

691 Grill-Spector, K., & Malach, R. (2004). The human visual cortex. *Annual review of neuroscience*, *27*,
692 649–677.

693 Grydeland, H., Walhovd, K. B., Tamnes, C. K., Westlye, L. T., & Fjell, A. M. (2013). Intracortical
694 myelin links with performance variability across the human lifespan: results from T1- and T2-
695 weighted MRI myelin mapping and diffusion tensor imaging. *The Journal of Neuroscience*, *33*(47),
696 18618–18630.

697 Haist, F., & Anzures, G. (2017). Functional development of the brain's face-processing system. *Wiley*
698 *interdisciplinary reviews. Cognitive science*, *8*(1-2).

699 Harkins, K. D., Dula, A. N., & Does, M. D. (2012). Effect of intercompartmental water exchange on
700 the apparent myelin water fraction in multiexponential T2 measurements of rat spinal cord.
701 *Magnetic resonance in medicine*, *67*(3), 793–800.

702 Hasson, U., Harel, M., Levy, I., & Malach, R. (2003). Large-Scale Mirror-Symmetry Organization of
703 Human Occipito-Temporal Object Areas. *Neuron*, *37*(6), 1027–1041.

704 Hodgetts, C. J., Shine, J. P., Lawrence, A. D., Downing, P. E., & Graham, K. S. (2016). Evidencing a
705 place for the hippocampus within the core scene processing network. *Human Brain Mapping*,
706 *37*(11), 3779–3794.

Hodgetts, C. J., Voets, N. L., Thomas, A. G., Clare, S., Lawrence, A. D., & Graham, K. S. (2017). Ultra-High-Field fMRI Reveals a Role for the Subiculum in Scene Perceptual Discrimination, *37*(12), 3150–3159.

Hutchison, R. M., Culham, J. C., Everling, S., Flanagan, J. R., & Gallivan, J. P. (2014). Distinct and distributed functional connectivity patterns across cortex reflect the domain-specific constraints of object, face, scene, body, and tool category-selective modules in the ventral visual pathway. *Neuroimage*, *96*, 216–236.

Jenkinson, M., Bannister, P., Brady, M., & Smith, S. M. (2002). Improved Optimization for the Robust and Accurate Linear Registration and Motion Correction of Brain Images. *Neuroimage*, *17*(2), 825–841.

Jenkinson, M., Beckmann, C. F., Behrens, T. E. J., Woolrich, M. W., & Smith, S. M. (2012). FSL. *Neuroimage*, *62*(2), 782–790.

Jenkinson, M., & Smith, S. M. (2001). A global optimisation method for robust affine registration of brain images. *Medical Image Analysis*, *5*(2), 143–156.

Jeurissen, B., Leemans, A., Tournier, J.-D., Jones, D. K., & Sijbers, J. (2013). Investigating the prevalence of complex fiber configurations in white matter tissue with diffusion magnetic resonance imaging. *Human Brain Mapping*, *34*(11), 2747–2766.

Jiang, P., Tokariev, M., Aronen, E. T., Salonen, O., Ma, Y., Vuontela, V., & Carlson, S. (2014). Responsiveness and functional connectivity of the scene-sensitive retrosplenial complex in 7-11-year-old children. *Brain and cognition*, *92C*, 61–72.

Jones, D. K., Horsfield, M. A., & Simmons, A. (1999). Optimal strategies for measuring diffusion in anisotropic systems by magnetic resonance imaging. *Magnetic resonance in medicine*, *42*(3), 515–525.

Jones, D. K., Knösche, T. R., & Turner, R. (2013). White matter integrity, fiber count, and other fallacies: the do's and don'ts of diffusion MRI. *Neuroimage*, *73*, 239–254.

732 Julian, J. B., Ryan, J., Hamilton, R. H., & Epstein, R. A. (2016). The Occipital Place Area Is Causally
733 Involved in Representing Environmental Boundaries during Navigation. *Current Biology*, *26*(8),
734 1104–1109.

735 Kalantari, S., Laule, C., Bjarnason, T. A., Vavasour, I. M., & MacKay, A. L. (2011). Insight into in
736 vivo magnetization exchange in human white matter regions. *Magnetic resonance in medicine*,
737 *66*(4), 1142–1151.

738 Koldewyn, K., Yendiki, A., Weigelt, S., Gweon, H., Julian, J., Richardson, H., et al. (2014).
739 Differences in the right inferior longitudinal fasciculus but no general disruption of white matter
740 tracts in children with autism spectrum disorder. *Proceedings of the National Academy of Sciences*
741 *of the United States of America*, *111*(5), 1981–1986.

742 Laule, C., Kozlowski, P., Leung, E., Li, D. K. B., MacKay, A. L., & Moore, G. R. W. (2008). Myelin
743 water imaging of multiple sclerosis at 7 T: correlations with histopathology. *Neuroimage*, *40*(4),
744 1575–1580.

745 Laule, C., Leung, E., Lis, D. K. B., Traboulsee, A. L., Paty, D. W., MacKay, A. L., & Moore, G. R.
746 W. (2006). Myelin water imaging in multiple sclerosis: quantitative correlations with
747 histopathology. *Multiple sclerosis*, *12*(6), 747–753.

748 Lebel, C., & Beaulieu, C. (2011). Longitudinal Development of Human Brain Wiring Continues from
749 Childhood into Adulthood. *The Journal of Neuroscience*, *31*(30), 10937–10947.

750 Levesque, I. R., & Pike, G. B. (2009). Characterizing healthy and diseased white matter using
751 quantitative magnetization transfer and multicomponent T(2) relaxometry: A unified view via a
752 four-pool model. *Magnetic resonance in medicine*, *62*(6), 1487–1496.

753 Loenneker, T., Klaver, P., Bucher, K., Lichtensteiger, J., Imfeld, A., & Martin, E. (2011).
754 Microstructural development: organizational differences of the fiber architecture between children
755 and adults in dorsal and ventral visual streams. *Human Brain Mapping*, *32*(6), 935–946.

756 MacKay, A. L., & Laule, C. (2016). Magnetic Resonance of Myelin Water: An in vivo Marker for
757 Myelin. *Brain plasticity*, *2*(1), 71–91.

758 MacKay, A. L., Whittall, K., Adler, J., Li, D. K. B., Paty, D., & Graeb, D. (1994). In vivo
759 visualization of myelin water in brain by magnetic resonance. *Magnetic resonance in medicine, 31*(6), 673–677.
760
761 Mackworth, N. H., & Bruner, J. S. (1970). How Adults and Children Search and Recognize Pictures.
762 *Human Development, 13*(3), 149–177.
763 McCarthy, P. (2018). FSLeyes. *Zenodo*.
764 Meissner, T. W., Genç, E., Mädler, B., & Weigelt, S. (2019a). Myelination of major white matter
765 tracts continues beyond childhood—combining tractography and myelin water imaging. *bioRxiv*,
766 from https://doi.org/10.1101/622233.
767 Meissner, T. W., Nordt, M., & Weigelt, S. (2019b). Prolonged functional development of the
768 parahippocampal place area and occipital place area. *Neuroimage, 191*, 104–115.
769 Meyers, S. M., Laule, C., Vavasour, I. M., Kolind, S. H., Mädler, B., Tam, R., et al. (2009).
770 Reproducibility of myelin water fraction analysis: a comparison of region of interest and voxel-
771 based analysis methods. *Magnetic resonance imaging, 27*(8), 1096–1103.
772 Miller, D. J., Duka, T., Stimpson, C. D., Schapiro, S. J., Baze, W. B., McArthur, M. J., et al. (2012).
773 Prolonged myelination in human neocortical evolution. *Proceedings of the National Academy of*
774 *Sciences of the United States of America, 109*(41), 16480–16485.
775 Miller, E. M. (1994). Intelligence and brain myelination: A hypothesis. *Personality and Individual*
776 *Differences, 17*(6), 803–832.
777 Moore, G. R. W., Leung, E., MacKay, A. L., Vavasour, I. M., Whittall, K. P., Cover, K. S., et al.
778 (2000). A pathology-MRI study of the short-T2 component in formalin-fixed multiple sclerosis
779 brain. *Neurology, 55*(10), 1506–1510.
780 Mori, S., & Tournier, J.-D. (2014). *Introduction to diffusion tensor imaging and higher order models*
781 (2nd edition). Boston: Academic Press.
782 Moura, L. M., Kempton, M., Barker, G., Salum, G., Gadelha, A., Pan, P. M., et al. (2016). Age-effects
783 in white matter using associated diffusion tensor imaging and magnetization transfer ratio during
784 late childhood and early adolescence. *Magnetic resonance imaging, 34*(4), 529–534.

785 Mukherjee, P., Chung, S. W., Berman, J. I., Hess, C. P., & Henry, R. G. (2008). Diffusion tensor MR
786 imaging and fiber tractography: technical considerations. *AJNR. American journal of*
787 *neuroradiology*, *29*(5), 843–852.

788 Mukherjee, P., Miller, J. H., Shimony, J. S., Conturo, T. E., Lee, B. C., Almli, C. R., & McKinstry, R.
789 C. (2001). Normal brain maturation during childhood: developmental trends characterized with
790 diffusion-tensor MR imaging. *Radiology*, *221*(2), 349–358.

791 Munsinger, H., & Gummerman, K. (1967). Identification of form in patterns of visual noise. *Journal*
792 *of Experimental Psychology*, *75*(1), 81–87.

793 Nordt, M., Semmelmann, K., Genç, E., & Weigelt, S. (2018). Age-related increase of image-
794 invariance in the fusiform face area. *Developmental cognitive neuroscience*, *31*, 46–57.

795 O'Craven, K. M., & Kanwisher, N. (2000). Mental imagery of faces and places activates
796 corresponding stiimulus-specific brain regions. *Journal of cognitive neuroscience*, *12*(6), 1013–
797 1023.

798 Oyefiade, A. A., Ameis, S., Lerch, J. P., Rockel, C., Szulc, K. U., Scantlebury, N., et al. (2018).
799 Development of short-range white matter in healthy children and adolescents. *Human Brain*
800 *Mapping*, *39*(1), 204–217.

801 Prasloski, T., Rauscher, A., MacKay, A. L., Hodgson, M., Vavasour, I. M., Laule, C., & Mädler, B.
802 (2012). Rapid whole cerebrum myelin water imaging using a 3D GRASE sequence. *Neuroimage*,
803 *63*(1), 533–539.

804 Pruessmann, K. P., Weiger, M., Scheidegger, M. B., & Boesiger, P. (1999). SENSE: Sensitivity
805 encoding for fast MRI. *Magnetic resonance in medicine*, *42*(5), 952–962.

806 Pujol, J., Soriano-Mas, C., Ortiz, H., Sebastián-Gallés, N., Losilla, J. M., & Deus, J. (2006).
807 Myelination of language-related areas in the developing brain. *Neurology*, *66*(3), 339–343.

808 R Core Team (2019). R: A Language and Environment for Statistical Computing, from
809 https://www.R-project.org.

Rollins, N. K., Glasier, P., Seo, Y., Morriss, M. C., Chia, J., & Wang, Z. (2010). Age-related variations in white matter anisotropy in school-age children. *Pediatric radiology*, *40*(12), 1918–1930.

Scherf, K. S., Thomas, C., Doyle, J., & Behrmann, M. (2014). Emerging structure-function relations in the developing face processing system. *Cerebral Cortex*, *24*(11), 2964–2980.

Ségonne, F., Dale, A. M., Busa, E., Glessner, M., Salat, D. H., Hahn, H. K., & Fischl, B. (2004). A hybrid approach to the skull stripping problem in MRI. *Neuroimage*, *22*(3), 1060–1075.

Sepehrband, F., Clark, K. A., Ullmann, J. F. P., Kurniawan, N. D., Leanage, G., Reutens, D. C., & Yang, Z. (2015). Brain tissue compartment density estimated using diffusion-weighted MRI yields tissue parameters consistent with histology, *36*(9), 3687–3702.

Shafee, R., Buckner, R. L., & Fischl, B. (2015). Gray matter myelination of 1555 human brains using partial volume corrected MRI images. *Neuroimage*, *105*, 473–485.

Smith, S. M. (2002). Fast robust automated brain extraction. *Human Brain Mapping*, *17*(3), 143–155.

Stanisz, G. J., Kecojevic, A., Bronskill, M. J., & Henkelman, R. M. (1999). Characterizing white matter with magnetization transfer and T(2). *Magnetic resonance in medicine*, *42*(6), 1128–1136.

Stikov, N., Perry, L. M., Mezer, A., Rykhlevskaia, E., Wandell, B. A., Pauly, J. M., & Dougherty, R. F. (2011). Bound pool fractions complement diffusion measures to describe white matter micro and macrostructure. *Neuroimage*, *54*(2), 1112–1121.

Takahashi, M., Hackney, D. B., Zhang, G., Wehrli, S. L., Wright, A. C., O'Brien, W. T., et al. (2002). Magnetic resonance microimaging of intraaxonal water diffusion in live excised lamprey spinal cord. *Proceedings of the National Academy of Sciences of the United States of America*, *99*(25), 16192–16196.

Tournier, J.-D., Calamante, F., & Connelly, A. (2009). How many diffusion gradient directions are required for HARDI? *Proceedings of the International Society for Magnetic Resonance in Medicine*, *17*, 358.

835 Tournier, J.-D., Calamante, F., Gadian, D. G., & Connelly, A. (2004). Direct estimation of the fiber
836 orientation density function from diffusion-weighted MRI data using spherical deconvolution.
837 *Neuroimage, 23*(3), 1176–1185.

838 van Wedeen, J., Hagmann, P., Tseng, W.-Y. I., Reese, T. G., & Weisskoff, R. M. (2005). Mapping
839 complex tissue architecture with diffusion spectrum magnetic resonance imaging. *Magnetic*
840 *resonance in medicine, 54*(6), 1377–1386.

841 Vass, L. K., & Epstein, R. A. (2013). Abstract representations of location and facing direction in the
842 human brain. *The Journal of Neuroscience, 33*(14), 6133–6142.

843 Vurpillot, E. (1968). The development of scanning strategies and their relation to visual
844 differentiation. *Journal of Experimental Child Psychology, 6*(4), 632–650.

845 Woolrich, M. W., Behrens, T. E. J., Beckmann, C. F., Jenkinson, M., & Smith, S. M. (2004).
846 Multilevel linear modelling for FMRI group analysis using Bayesian inference. *Neuroimage, 21*(4),
847 1732–1747.

848 Woolrich, M. W., Ripley, B. D., Brady, M., & Smith, S. M. (2001). Temporal autocorrelation in
849 univariate linear modeling of FMRI data. *Neuroimage, 14*(6), 1370–1386.

850 Yakovlev, P. I., & Lecours, A.-R. (1967). The myelogenetic cycles of regional maturation of the brain.
851 In A. Minkowski (Ed.), *Regional Development of the Brain Early in Life* (pp. 3–70). Boston, MA:
852 Blackwell Scientific Publications Inc.

853 Yeatman, J. D., Dougherty, R. F., Ben-Shachar, M., & Wandell, B. A. (2012). Development of white
854 matter and reading skills. *Proceedings of the National Academy of Sciences of the United States of*
855 *America, 109*(44), E3045-53.

856 Yendiki, A., Panneck, P., Srinivasan, P., Stevens, A., Zöllei, L., Augustinack, J., et al. (2011).
857 Automated probabilistic reconstruction of white-matter pathways in health and disease using an
858 atlas of the underlying anatomy. *Frontiers in Neuroinformatics, 5*, 23.

859 Zatorre, R. J., Fields, R. D., & Johansen-Berg, H. (2012). Plasticity in gray and white: neuroimaging
860 changes in brain structure during learning. *Nature neuroscience, 15*(4), 528–536.

Zeidman, P., Mullally, S. L., & Maguire, E. A. (2015). Constructing, Perceiving, and Maintaining Scenes: Hippocampal Activity and Connectivity. *Cerebral Cortex, 25*(10), 3836–3855.